Microfocus Laser–Angle-Resolved Photoemission on Encapsulated Mono-, Bi-, and Few-Layer 1T′-WTe_2

Cucchi, Irène; Gutierrez Lezama, Ignacio; Cappelli, Edoardo; Mckeown Walker, Siobhan; Bruno, Flavio Yair; Tenasini, Giulia; Wang, Lin; Ubrig, Nicolas; Barreteau, Céline; Giannini, Enrico; Gibertini, Marco; Tamai, Anna; Morpurgo, Alberto; Baumberger, Felix

How to cite

CUCCHI, Irène et al. Microfocus Laser–Angle-Resolved Photoemission on Encapsulated Mono-, Bi-, and Few-Layer 1T′-WTe_2. In: Nano Letters, 2018. doi: 10.1021/acs.nanolett.8b04534

This publication URL: https://archive-ouverte.unige.ch/unige:112585

Publication DOI: 10.1021/acs.nanolett.8b04534

Microfocus laser-ARPES on encapsulated mono-, bi- and few-layer 1T'-WTe$_2$

Journal:	*Nano Letters*
Manuscript ID	nl-2018-04534y.R1
Manuscript Type:	Communication
Date Submitted by the Author:	12-Dec-2018
Complete List of Authors:	Cucchi, Irène; Université de Genève, Department of Quantum Matter Physics Gutiérrez, Ignacio; Université de Genève, Department of Quantum Matter Physics Cappelli, Edoardo; Université de Genève, Department of Quantum Matter Physics Mckeown Walker, Siobhan; Universite de Geneve Bruno, Flavio; Universite de Geneve, Tenasini, Giulia; Université de Genève, Department of Quantum Matter Physics Wang, Lin; Universite de Geneve, Ubrig, Nicolas; Universite de Geneve, Department of quantum matter physics Barreteau, Céline; Université de Genève, Department of Quantum Matter Physics Giannini, Enrico; Universite de Geneve, Département de Physique de la Matière Condensée Gibertini, Marco; Université de Genève, Department of Quantum Matter Physics Tamai, Anna; Université de Genève, Department of Quantum Matter Physics Morpurgo, Alberto; DPMC and GAP University of Geneva, Baumberger, Felix ; Universite de Geneve,

Microfocus laser-ARPES on encapsulated mono-, bi- and few-layer 1T'-WTe_2

Irène Cucchi,[†] Ignacio Gutiérrez-Lezama,[†,‡] Edoardo Cappelli,[†] Siobhan McKeown Walker,[†] Flavio Y. Bruno,[†] Giulia Tenasini,[†,‡] Lin Wang,[†,‡,‖] Nicolas Ubrig,[†,‡] Céline Barreteau,[†,⊥] Enrico Giannini,[†] Marco Gibertini,[†,¶] Anna Tamai,[†] Alberto F. Morpurgo,[†,‡] and Felix Baumberger*[,†,§]

†*Department of Quantum Matter Physics, University of Geneva, 24 quai Ernest Ansermet, CH-1211 Geneva, Switzerland*

‡*Group of Applied Physics, University of Geneva, 24 Quai Ernest Ansermet, CH-1211 Geneva, Switzerland*

¶*National Centre for Computational Design and Discovery of Novel Materials (MARVEL), École Polytechnique Fédérale de Lausanne, CH-1015 Lausanne, Switzerland*

§*Swiss Light Source, Paul Scherrer Institute, CH-5232 Villigen, Switzerland*

‖*Current address: Key Laboratory of Flexible Electronics (KLOFE) & Institute of Advanced Materials (IAM), Jiangsu National Synergetic Innovation Center for Advanced Materials (SICAM), Nanjing Tech University (Nanjing Tech), 30 South Puzhu Road, Nanjing 211816, China*

⊥*Current address: Institut de Chimie et des Matériaux Paris Est - UMR 7182, 2-8 rue H. Dunant 94320 THIAIS, France*

E-mail: Felix.Baumberger@unige.ch

Abstract

Two-dimensional crystals of semimetallic van der Waals materials hold much potential for the realization of novel phases, as exemplified by the recent discoveries of a polar metal in few layer 1T'-WTe_2 and of a quantum spin Hall state in monolayers of the same material. Understanding these phases is particularly challenging because little is known from experiment about the momentum space electronic structure of ultrathin crystals. Here, we report direct electronic structure measurements of exfoliated mono- bi- and few-layer 1T'-WTe_2 by laser-based micro-focus angle resolved photoemission. This is achieved by encapsulating with monolayer graphene a flake of WTe_2 comprising regions of different thickness. Our data support the recent identification of a quantum spin Hall state in monolayer 1T'-WTe_2 and reveal strong signatures of the broken inversion symmetry in the bilayer. We finally discuss the sensitivity of encapsulated samples to contaminants following exposure to ambient atmosphere.

Keywords

van der Waals heterostructures, electronic structure, nano-ARPES, 1T'-WTe2

Main

Two-dimensional (2D) van der Waals (vdW) materials host fascinating phases of quantum matter. A particularly striking example is WTe_2. In the bulk, its most stable 1T' structure has a non-symmorphic space group ($Pnm2_1$), shows giant non-saturating magnetoresistance,[1] pressure induced superconductivity[2,3] and has been proposed as a candidate type-II Weyl semimetal,[4] although the latter has not been confirmed experimentally to date.[5,6] Exfoliated crystals remain metallic down to 3 Te-W-Te units when encapsulated in hexagonal boron nitride (h-BN)[7,8] [1]. The monolayer (ML) is a robust 2D topological insulator with

[1]The bulk primitive unit cell of 1T'-WTe_2 contains 2 Te-W-Te layers and 4 formula units. However, the thickness of thin samples is given in the literature and throughout this paper in multiples of individual Te-W-Te trilayers.

helical edge modes producing a quantum spin Hall state[7,9–13] and becomes superconducting when doped electrostatically.[14,15] The bilayer (BL) is a topologically trivial ferroelectric insulator at low temperature and becomes metallic above $\sim$ 20 K while retaining a finite polarization.[7,16] Spontaneous electrical polarization, switchable with a gate field, was also found in trilayer samples where it coexists with metallic conductivity at low temperature.[16]

Understanding the emergence of these properties as the thickness is reduced towards a single ML is challenging, in part because many of the powerful experimental tools developed for the study of bulk single crystals currently lack the sensitivity to be applied to a single exfoliated flake of a few micron lateral dimension. Angle resolved photoemission (ARPES), arguably the most direct probe of the electronic band structure, is an exception in the sense that it is, at least in principle, sensitive to a single ML. Studying 2D van der Waals materials by ARPES proved challenging though. One approach is the *in-situ* deposition of vdW materials, which produces large samples, compatible with standard high-resolution ARPES instruments. While this has been used successfully to study several transition metal dichalcogenide (TMD) ML systems,[10,17] the deposition of multilayer TMDs or heterostructures is often not possible. Moreover, epitaxial growth limits the number of substrates and generally results in multiple structural domains, which complicates the interpretation of momentum space resolved but real space averaging measurements.[10] Alternatively, several groups have used synchrotron based micro-focus ARPES on samples prepared by *ex-situ* micromechanical exfoliation of bulk crystals.[18–22] However, little is known about methods to prepare suitable samples with a surface quality rivaling that of bulk single crystals cleaved in ultra-high vacuum (UHV). To date μ-ARPES experiments have been limited to a few semiconducting TMDs, which are stable in air and can be annealed at high temperature to clean the surface.[18–22] This approach facilitates the preparation of samples but is not readily applicable to semimetallic TMDs such as 1T'-WTe_2, superconductors and density wave systems such as FeSe or $NbSe_2$ or topical vdW magnets such as CrI_3, which all are too reactive and/or decompose at high temperature.

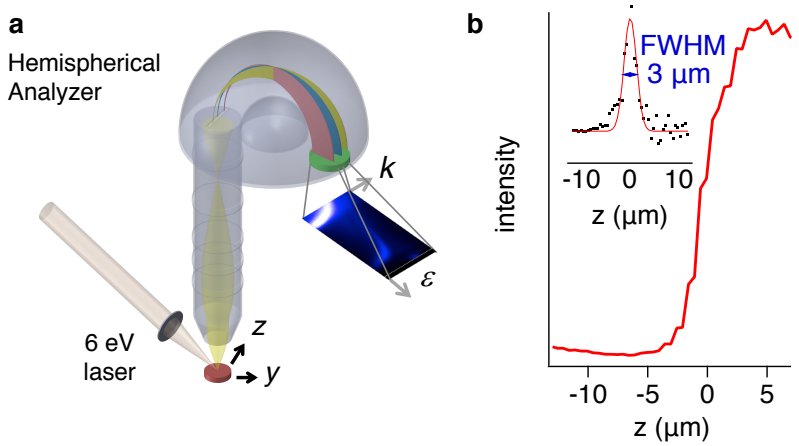

Figure 1: (a) Sketch of the μ-ARPES setup. For details, see main text. (b) Knife edge scan across the sharp transition from the SiO_2 substrate to a Au contact. The inset shows the derivative of the line scan with a Gaussian fit indicating a full width half maximum (FWHM) of ~ 3 μm.

Here, we report laser-based μ-ARPES experiments on exfoliated flakes of the reactive semimetal 1T'-WTe_2. We show that encapsulation of a flake with ML graphene under protective atmosphere provides ARPES data of a quality comparable to that of bulk single crystals cleaved in UHV. We clearly resolve the inverted band gap underlying the quantum spin Hall state in ML 1T'-WTe_2 and find a strong Rashba-like spin-splitting in the BL arising from its broken inversion symmetry. Our results further demonstrate that laboratory based μ-ARPES instruments are a promising alternative to micro-focus synchrotron beamlines.

The ARPES measurements reported here were performed in a custom built micro-ARPES system illustrated schematically in Fig. 1(a). A continuous wave laser source from LEOS solutions providing up to 10^{15} photons/s with 206 nm wavelength (6.01 eV) in a μeV bandwidth was used as excitation source. The laser beam was first expanded and then refocused using a 1" aberration corrected lens with ~ 65 mm focal lenght mounted in UHV on a motorized 3-axes translator. Photoelectrons were collected and analyzed with an MB Scientific hemispherical analyzer equipped with a deflector lens capable of acquiring 2D k-space maps without rotating the sample. Typical energy and momentum resolutions were 0.003 $Å^{-1}$ / 2 meV. Samples have been mounted on a conventional 6-axes ARPES manipulator described

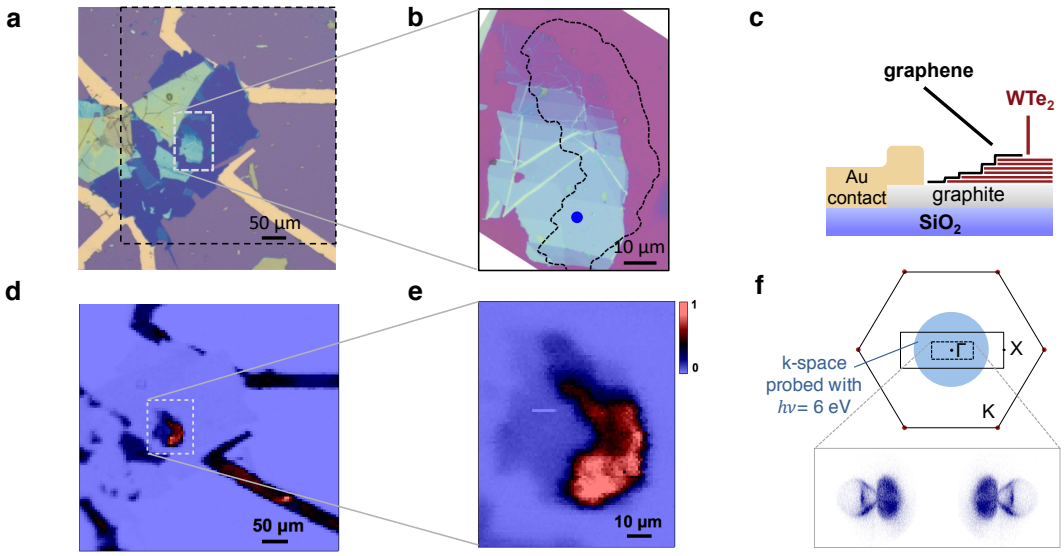

Figure 2: (a) Micrograph of the full assembly with Au contacts (yellow), graphite bottom electrode (blue) and different WTe_2 flakes (turquoise) on the SiO_2 substrate (violet). (b) Zoom-in showing the encapsulated flake in the area marked by a dashed white line in (a). The boundary of the graphene encapsulation layer is shown by a black dotted line. The blue circle with 3 μm diameter illustrates the spatial resolution of the μ-ARPES experiments. (c) Schematic of the sample studied in this work. (d) Scanned μ-ARPES image of the area marked by the black dashed rectangle in (b). (e) Magnified μ-ARPES image of the partially encapsulated WTe_2 flake (dashed grey rectangle in (d)). (f) Brillouin zone of bulk 1T'-WTe_2 (black rectangle) and graphene (hexagon). The magnified inset shows the Fermi surface of cleaved bulk 1T'-WTe_2 measured with $h\nu = 6$ eV.

in Ref.[23] All experiments were performed at pressures $< 10^{-10}$ mbar and a manipulator temperature of ~ 4.5 K measured on the sample receptacle. The actual temperature of the exfoliated flake determined from the width of the Fermi cutoff was in the range of $30-40$ K. Sample positions were scanned with a stepper motor driven xyz-stage with 100 nm resolution and < 1 μm bidirectional reproducibility. The effective spatial resolution of the system has been determined from line scans across Au contacts on a SiO_2 substrate. As shown in Fig. 1(b), this indicates a resolution of 3 μm. Drift of the sample position was found to be significant during cool down but negligible in thermal equilibrium.

Optical micrographs and the schematic configuration of the vdW heterostructure used for our experiments are shown in Fig. 2(a-c). A graphite bottom electrode is placed on

a SiO_2 wafer and contacted with Ti/Au lines defined with conventional nano-fabrication techniques to ground the assembly. The bottom electrode provides at the same time an atomically flat surface with minimal contamination from adsorbates. WTe_2 crystals were synthesized with the chemical vapor transport (CVT) method [24] and exfoliated onto a Si/SiO_2 substrate in the protective atmosphere of a glovebox with sub-ppm contamination of water and a concentration of O_2 below 20 ppm. For our experiments, we isolated the flake shown in Fig. 2(b) whose thickness determined from the optical contrast on SiO_2 ranges from a single ML to $\sim$ 12 nm. The WTe_2 flake was then picked up with a graphene ML on a PC/PDMS stamp and transfered onto the bottom graphite electrode using an all-dry transfer method. [25,26] This ensures that the interface between WTe_2 and the encapsulating graphene ML is free from PC residues. The relative orientation between the thick bottom graphite electrode, the WTe_2 flake and the graphene ML used to encapsulate it was not controlled. More details about the fabrication of the vdW heterostructure are provided in supplementary information. The assembled heterostructure was transported under glovebox atmosphere to the ARPES system using a specially designed suitcase and pumped down to UHV pressures without ever exposing it to ambient air. The sample was neither annealed nor cleaned in any other way prior to the first ARPES measurements. The thickness of the relevant areas of the WTe_2 flake determined from the optical contrast was confirmed after the μ-ARPES experiments using *ex-situ* atomic force microscopy (supplementary figure S2).

Fig. 2(d) demonstrates imaging of the full assembly by laser-based μ-ARPES. Scanning the sample while collecting photoelectrons near normal emission with energies within 0.3 eV from the Fermi level shows high contrast between the Au contact lines and the SiO_2 substrate. High intensity is also observed for the encapsulated part of the WTe_2 flake (marked by a black line in Fig. 2(b)) providing a first indication for the effective protection of its low-energy electronic states. The graphene encapsulation layer, on the other hand, is completely invisible in our μ-ARPES images and even the thick graphite bottom electrode shows minimal intensity. This is a direct consequence of the energy and momentum space resolution of

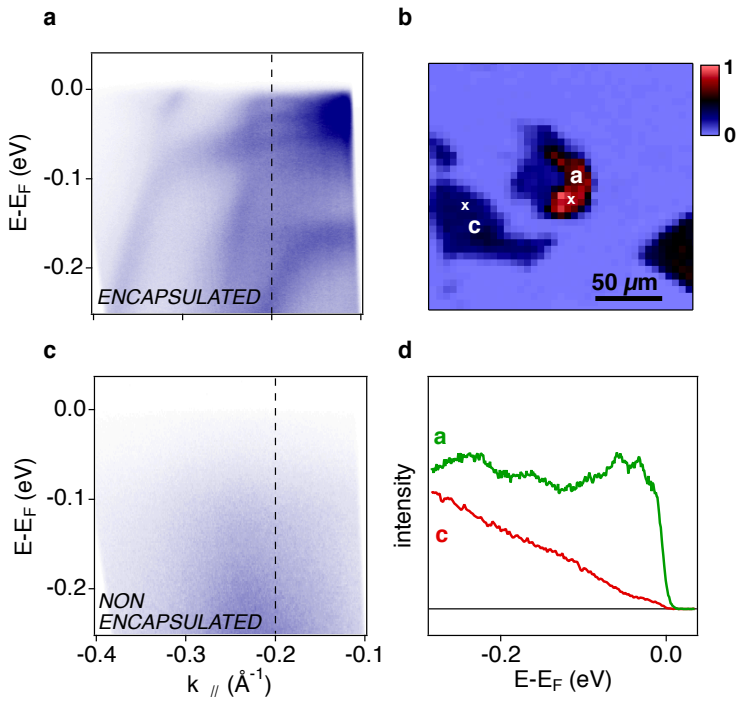

Figure 3: Effect of encapsulation on the electronic states. (a) Band dispersion of encapsulated mulitlayer 1T'-WTe_2 along ΓX measured at the position indicated in the real space image shown in (b). (c) μ-ARPES data acquired under identical conditions on a non-encapsulated flake of similar thickness at the position indicated in (b). (d) Energy distribution curves at $k_{\|} = 0.2$ Å^{-1} (black dashed line) extracted from the data in (a), (c).

ARPES. As shown in Fig. 2(f), the Fermi surface of 1T'-WTe_2 is well separated in k-space from the low-energy electronic states of graphene at the K-points. Moreover, within the momentum space accessible at 6 eV photon energy, the lowest lying graphene excitations arise from the σ-band located several eV below the chemical potential. Direct transitions from graphene or graphite initial states are thus not possible within the entire energy and momentum range probed in our experiments. The large separation of WTe_2 and graphene states in momentum space will also reduce hybridization of initial states not probed in our experiment.

The effect of encapsulation is demonstrated directly in Fig. 3, where we compare μ-ARPES data from the bulk-like part of the encapsulated WTe_2 flake with data from a different flake of similar thickness that was not encapsulated. The data taken on encapsulated WTe_2 show multiple well defined dispersive states with an overall data quality that

is comparable to high-resolution ARPES data from cleaved bulk samples.[5,27] In contrast, the non-encapuslated flake shows a largely featureless ARPES spectrum with strongly reduced intensity at the chemical potential as it is typical for the heavily contaminated surface of bulk WTe_2. This is remarkable, considering that both flakes were exposed to the same environment and implies an effective protection of the encapsulated flake and/or an active self-cleansing effect during the encapsulation with graphene.[25,28]

Having demonstrated well defined electronic states in encapsulated flakes, we proceed to investigate the electronic structure of ML and BL 1T'-WTe_2 (Fig. 4). Corresponding regions were identified in the optical micrograph, as indicated in Fig. 4(b), and measured for two different polar angles to cover an extended k-space range. We start by discussing the ML data. The primitive unit cell of bulk 1T'-WTe_2 contains two WTe_2 layers. Isolating a single ML will thus profoundly change the symmetry and electronic structure. Most importantly, a ML is inversion symmetric, whereas all multilayers lack an inversion center. This causes a relatively simple electronic structure with spin-degenerate states in the ML. Our data in Fig. 4(c) show two fully occupied hole like bands and small electron pockets at $k_x \approx \pm 0.3$ Å^{-1} that barely touch the chemical potential. From our density functional theory (DFT) calculations, we identify these states with the conduction band minimum (CBM) formed by a combination of d_{yz} orbitals on the W atoms with positive overall parity (d^+_{yz}), the d^+_{xz} valence band maximum (VBM), and a $d^-_{z^2}$ state (with negative parity) at ~ -0.55 eV, in agreement with earlier theoretical work and an ARPES study on MBE grown films[9,10,31] [2]. This confirms the $d-d$ inversion of bands with opposite parity[31] causing the spin-momentum locked topological edge states of ML 1T'-WTe_2.[7,10–12] In supplementary Fig. S4, we directly confirmed edge conduction on samples exfoliated from the same set of crystals.

From fits of energy distribution curves we determine a CBM in our ML sample of $-9(5)$ meV and a VBM of $-75(5)$ meV. We thus estimate a gap of 66(7) meV, slightly

[2]Note that we define the shortest lattice vector along x, as it is also done in Refs.[9,31] Hence, we denote the long axis of the Brillouin zone by ΓX, whereas Ref.[10] defines this direction as ΓY. This rotation of the coordinate system further transforms xz into yz orbitals and vice versa

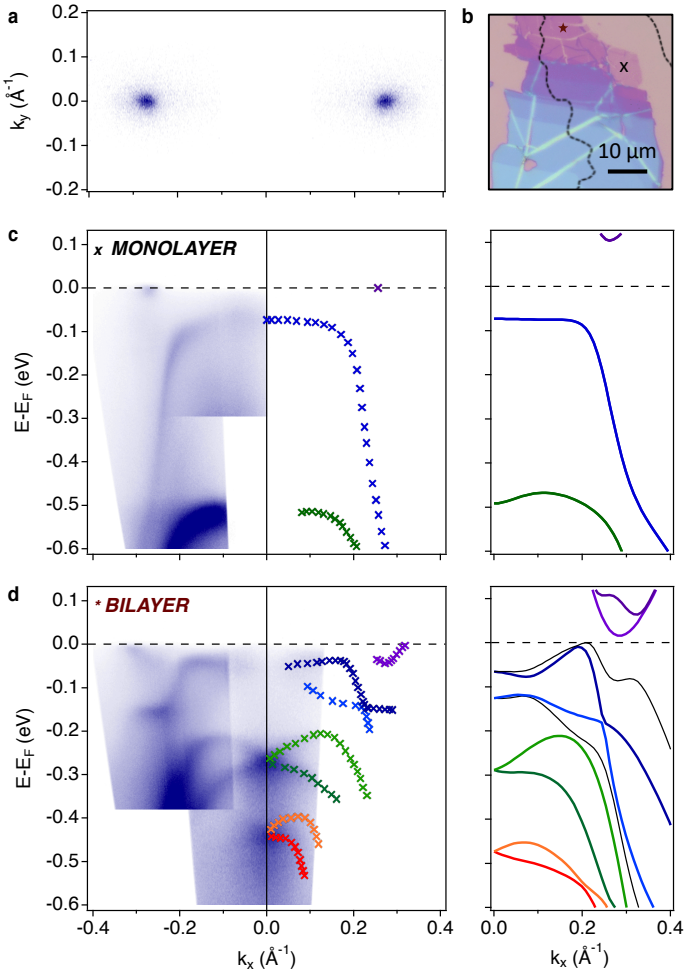

Figure 4: Electronic structure of ML and BL 1T'-WTe_2. (a) Fermi surface of ML 1T'-WTe_2. (b) Micrograph of WTe_2 as exfoliated on SiO_2. The black dotted line marks the part of the flake that has been encapsulated with monolayer graphene. (c,d) Band dispersion along ΓX taken in the ML and BL regions of the sample marked by a black cross and dark red star in (b), respectively. The abrupt breaks in contrast in the false color plots arise from combining data taken with different light polarization and in different experimental geometries. The ML was measured with s-polarization at high $k_{||}$ and p-polarization near normal emission, while both data sets merged to obtain the BL dispersion were taken with s-polarization. Band dispersions extracted from multiple experiments including data sets not shown in the paper are indicated with crosses and colored to facilitate comparison with the DFT band structures shown on the right. DFT calculations have been performed for isolated ML and BL with the Heyd–Scuseria–Ernzerhof hybrid functional[29] as implemented in the VASP code[30] (see supplementary information for more details).

larger than the 55 meV reported in MBE grown films.[10] Because of the very small Fermi energy in our sample we cannot directly resolve distinct Fermi crossings within a single conduction band pocket. We thus estimate an upper bound of the carrier density from the half width at half maximum of the momentum distribution curve at the chemical potential which must be greater than the Fermi wave vector k_F (see supplementary Fig. S3). This gives a carrier density $n_{2D} = k_F^2/\pi < 10^{12}$ cm^{-2} for the 2 nearly isotropic spin-degenerate conduction band pockets. The origin of this slight n-type doping is presently unknown. We note, however, that the above carrier density of $n_{2D} < 10^{12}$ cm^{-2} is below the onset of conduction reported in Ref.[7] Moreover, the position of the chemical potential at the conduction band edge in our data is consistent with transport experiments in WTe_2 encapsulated in hexagonal boron nitride (Ref.[7] and supplementary Fig. S4). This suggest that the slight n-type doping of our WTe_2 sample is not dominated by charge transfer from graphene.

BL 1T'-WTe_2 is the first atomically thin vdW material showing ferroelectric polarization. Although the origin of ferroelectricity is not fully established yet, transport evidence points to an important role of itinerant electronic states.[16] A characterization of the electronic band structure of BL 1T'-WTe_2 is thus of particular interest. This can readily be achieved on our encapsulated sample, which has a BL region of several microns lateral dimension but would be difficult by any other means. Remarkably, our μ-ARPES data from the BL shows a surprisingly rich band structure, which cannot be approximated starting from the ML band structure by introducing a simple splitting into bonding and antibonding states. We attribute the additional complexity in the band structure predominantly to the strong effects of inversion symmetry breaking in BL 1T'-WTe_2, which lifts the spin degeneracy. Together with the doubling of the unit cell, one thus expects a four fold increase in the number of bands. This is indeed evident in the calculation, which shows 8 valence bands in the energy range of the two highest valence bands of the ML. The strong effect of the inversion symmetry breaking is most striking in the doublet colored in green, which shows the characteristic crossing of Rashba spin-split bands, imposed by the Kramers degeneracy at

the time reversal invariant Γ point. We note that not all bands predicted by the calculation are detected in experiment. This can be attributed to matrix element effects and is not unusual in ARPES.

Compared to the ML, we find a strongly increased carrier density of $n_{2D} \approx 3.6 \cdot 10^{12}$ cm^{-2} and a vanishing, if not slightly negative gap. While the origin of these changes are not clear yet, we note that our observations are consistent with the onset of metallic conductivity above ~ 20 K[7] considering that the actual sample temperature in our experiments is in the range of $30 - 40$ K. We remark, however, that the size and nature of the gap in ML and BL 1T'-WTe_2 is not yet established conclusively. DFT calculations in the generalized gradient approximation show a band overlap in both cases (see supplementary Fig. S5). This can be rectified, as done here, by using a hybrid functional providing a more realistic description of electron correlations. While such calculations reproduce the overall band structure, as shown in Fig. 4, quantitative discrepancies remain. Most notably, our hybrid functional calculations overestimate the gap in ML 1T'-WTe_2 seen in ARPES by about a factor of two. Together with the abrupt closure of the gap at relatively low temperature reported in Ref.,[7] this suggests a non-negligible and not yet fully understood role of many-body interactions. We also point out that the gap is affected by slight changes in the crystal structure (see Fig. S5) or by vertical electric fields, which depend on the encapsulating material and are hard to fully eliminate in experiments. Such field effects should be particularly pronounced in the BL with its strong inversion symmetry breaking and electrical polarization.

In Fig. 5, we investigate the robustness of our sample design against aging. To this end, we reproduce the μ-ARPES data of bulk like encapsulated WTe_2 from Fig. 3(a) and compare them with spectra taken at the same position following exposure to ambient atmosphere. The contact with air causes clear degradation in the form of a sizeable broadening of the spectra although we find remnants of the pristine band structure even after exposure to air for 24 h (panel (d)). Remarkably, the electronic structure of the encapsulated sample recovers almost completely after mild annealing in UHV (2' at 210° C). This is in sharp

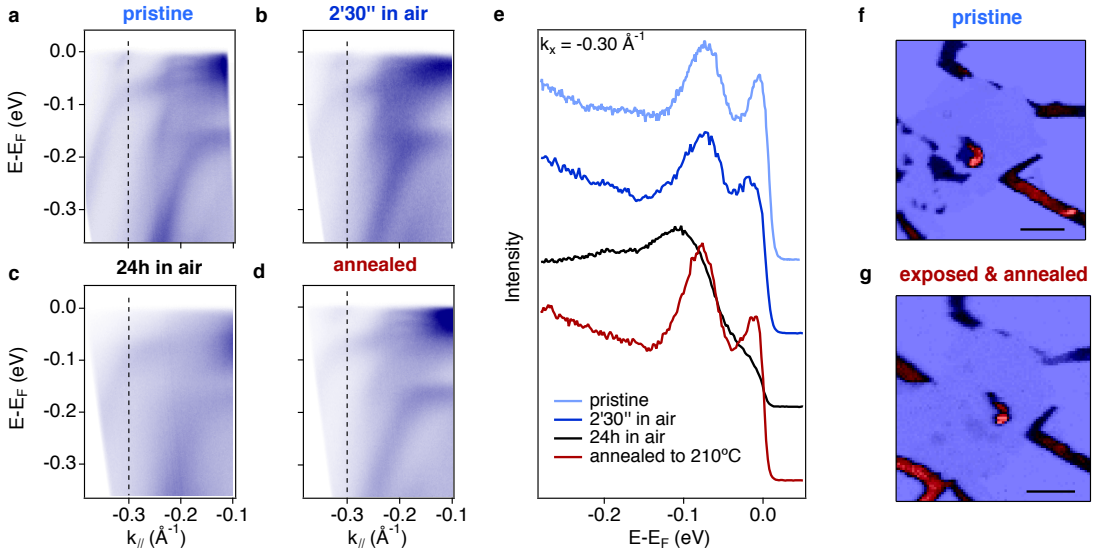

Figure 5: (a-d) μ-ARPES band structure measurements of encapsulated multilayer 1T'-WTe_2, compared to data taken at the same position after exposure of the full assembly to air and subsequent annealing at 210° C. (e) Energy dispersion curves at $k_{||} = -0.3$ Å^{-1} extracted from the data sets in (a-d). (f,g) Real-space μ-ARPES images of the pristine sample and of the same area after exposure to air and annealing in UHV. The length of the scale bar is 100 μm.

contrast to the behavior of the exposed surface of WTe_2 reported in Ref.[32] The irreversible and almost complete degradation of non-encapsulated WTe_2 during a cycle of exposure to air and subsequent annealing is also evident in the spatial maps of the low-energy spectral weight shown in Fig. 5(f,g). On the pristine sample (Fig. 5(f)), we detect signal from the entire WTe_2 flake studied in Figs. 2-5, including its non-encapsulated part, as well as from multiple other non-encapsulated flakes, whereas at the end of the cycle, significant intensity is observed only for the Au contacts and the encapsulated part of the WTe_2 (Fig. 5(g)).

Our μ-ARPES data from the pristine encapulated flake show typical linewidths of $\sim$ 30 meV, which compares favorably to MBE grown films[10] and to μ-ARPES studies of much more inert semiconducting TMDs.[18–22] We partially attribute this to the self-cleansing effect between two atomically flat surfaces when 2D materials have a high affinity reported before.[25,28] This interpretation is supported by our AFM images, which show bright white spots that are suspected to be pockets of trapped contaminants pushed away during the encapsulation

to leave extended interfaces between the TMD and graphene atomically clean. The highly reversible behavior in exposure / annealing cycles further demonstrates that encapsulation with graphene largely prevents oxidation of WTe_2 observed in ambient air[33] and suggests that the predominant broadening mechanism following exposure to air is a long-range chemical potential variation caused by charged, weakly-bound contaminants on the surface of graphene, which can be desorbed in UHV by mild annealing. We finally note that the data quality obtained on bulk-like encapsulated WTe_2 showed no signs of degradation over several months in UHV including more than a dozen temperature cycles between liquid helium and room temperature. This is in strong contrast to typical lifetimes of cleaved bulk samples for conventional ARPES experiments of 12-24 hours.

In conclusion, we have demonstrated that encapsulation of 1T'-WTe_2 with graphene is suitable to obtain high-quality electronic structure data using μ-ARPES. This opens the way for electronic structure measurements on a broad range of previously inaccessible ultrathin TMDs including 2D magnets, charge density wave systems and superconductors such as FeSe or $NbSe_2$, on exfoliated Dirac and Weyl semimetals, or on reactive 2D semiconductors such as phosphorene. In addition, we showed that the use of deep UV lasers is a promising alternative to synchrotron-based μ-ARPES. Together, these advances should promote a more widespread use of ARPES in the study of 2D TMDs and heterostructures thereof.

Acknowledgement

We gratefully acknowledge discussions with David Cobden, Hugo Henck, Simone Lisi and Sara Riccò. This work was supported by the Swiss National Science Foundation (SNSF) Div. II, the SNSF Synergia program, the NCCR QSIT and the EU Graphene Flagship. MG and NU were supported by SNSF Ambizione fellowships. Simulation time was provided by CSCS on Piz Daint (project id s825).

Supporting Information Available

Additional details and figures on sample fabrication and characterization, supporting analysis of ARPES data, confirmation of edge conduction in transport measurements and additional DFT calculations.

References

(1) Ali, M. N.; Xiong, J.; Flynn, S.; Tao, J.; Gibson, Q. D.; Schoop, L. M.; Liang, T.; Haldolaarachchige, N.; Hirschberger, M.; Ong, N. P.; Cava, R. J. Large, non-saturating magnetoresistance in WTe 2. *Nature* **2014**, *514*, 205.

(2) Kang, D.; Zhou, Y.; Yi, W.; Yang, C.; Guo, J.; Shi, Y.; Zhang, S.; Wang, Z.; Zhang, C.; Jiang, A., S.and Li; Yang, K.; Wu, Q.; Zhang, G.; Sun, L.; Zhao, Z. Superconductivity emerging from a suppressed large magnetoresistant state in tungsten ditelluride. *Nature Communications* **2015**, *6*, 7804.

(3) Pan, X. C.; Chen, X.; Liu, H.; Feng, Y.; Wei, Z.; Zhou, Y.; Chi, Z.; Pi, L.; Yen, F.; Song, F.; Wan, X.; Yang, Z.; Wang, B.; Wang, G.; Zhang, Y. Pressure-driven dome-shaped superconductivity and electronic structural evolution in tungsten ditelluride. *Nature Communications* **2015**, *6*, 7805.

(4) Soluyanov, A. A.; Gresch, D.; Wang, Z.; Wu, Q.; Troyer, M.; Dai, X.; Bernevig, B. A. Type-II Weyl semimetals. *Nature* **2015**, *527*, 495–8.

(5) Bruno, F. Y. et al. Observation of large topologically trivial Fermi arcs in the candidate type-II Weyl semimetal WT e2. *Physical Review B* **2016**, *94*, 121112.

(6) Armitage, N. P.; Mele, E. J.; Vishwanath, A. Weyl and Dirac semimetals in three-dimensional solids. *Rev. Mod. Phys.* **2018**, *90*, 015001.

(7) Fei, Z.; Palomaki, T.; Wu, S.; Zhao, W.; Cai, X.; Sun, B.; Nguyen, P.; Finney, J.; Xu, X.; Cobden, D. H. Edge conduction in monolayer WTe2. *Nature Physics* **2017**, *13*, 677–682.

(8) Fatemi, V.; Gibson, Q. D.; Watanabe, K.; Taniguchi, T.; Cava, R. J.; Jarillo-Herrero, P. Magnetoresistance and quantum oscillations of an electrostatically tuned semimetal-to-metal transition in ultrathin WTe2. *Physical Review B* **2017**, *95*, 41410.

(9) Qian, X.; Liu, J.; Fu, L.; Li, J. Quantum spin Hall effect in two-dimensional transition metal dichalcogenides. *Science* **2014**, *346*, 1344–7.

(10) Tang, S. et al. Quantum spin Hall state in monolayer 1T'-WTe2. *Nature Physics* **2017**, *13*, 683–687.

(11) Wu, S.; Fatemi, V.; Gibson, Q. D.; Watanabe, K.; Taniguchi, T.; Cava, R. J.; Jarillo-Herrero, P. Observation of the Quantum Spin Hall Effect up to 100 Kelvin in a Monolayer. *Science* **2018**, *359*, 76–79.

(12) Shi, Y.; Kahn, J.; Niu, B.; Fei, Z.; Sun, B.; Cai, X.; Francisco, B. A.; Wu, D.; Shen, Z.-X.; Xu, X.; Cobden, D. H.; Cui, Y.-T. Imaging Quantum Spin Hall Edges in Monolayer WTe2. *arXiv:1807.09342* **2018**,

(13) Xu, S. Y. et al. Electrically switchable Berry curvature dipole in the monolayer topological insulator WTe2. *Nature Physics* **2018**, *14*, 900.

(14) Sajadi, E.; Palomaki, T.; Fei, Z.; Zhao, W.; Bement, P.; Olsen, C.; Luescher, S.; Xu, X.; Folk, J. A.; Cobden, D. H. Gate-induced superconductivity in a monolayer topological insulator. *Science* **2018**,

(15) Fatemi, V.; Wu, S.; Cao, Y.; Bretheau, L.; Gibson, Q. D.; Watanabe, K.; Taniguchi, T.; Cava, R. J.; Jarillo-Herrero, P. Electrically tunable low-density superconductivity in a monolayer topological insulator. *Science* **2018**,

(16) Fei, Z.; Zhao, W.; Palomaki, T. A.; Sun, B.; Miller, M. K.; Zhao, Z.; Yan, J.; Xu, X.; Cobden, D. H. Ferroelectric switching of a two-dimensional metal. *Nature* **2018**, *560*, 336.

(17) Zhang, Y.; Chang, T.; Zhou, B.; Cui, Y. Direct observation of the transition from indirect to direct bandgap in atomically thin epitaxial MoSe2. *Nat. Nanotechnol.* **2013**, *9*, 111–115.

(18) Jin, W.; Yeh, P. C.; Zaki, N.; Zhang, D.; Sadowski, J. T.; Al-Mahboob, A.; Van Der Zande, A. M.; Chenet, D. A.; Dadap, J. I.; Herman, I. P.; Sutter, P.; Hone, J.; Osgood, R. M. Direct measurement of the thickness-dependent electronic band structure of MoS2 using angle-resolved photoemission spectroscopy. *Physical Review Letters* **2013**, *111*, 106801.

(19) Coy Diaz, H.; Avila, J.; Chen, C.; Addou, R.; Asensio, M. C.; Batzill, M. Direct observation of interlayer hybridization and dirac relativistic carriers in Graphene/MoS2van der waals heterostructures. *Nano Letters* **2015**, *15*, 1135–1140.

(20) Yuan, H. et al. Evolution of the Valley Position in Bulk Transition-Metal Chalcogenides and Their Monolayer Limit. *Nano Letters* **2016**, *16*, 4738–4745.

(21) Pierucci, D.; Henck, H.; Avila, J.; Balan, A.; Naylor, C. H.; Patriarche, G.; Dappe, Y. J.; Silly, M. G.; Sirotti, F.; Johnson, A. T.; Asensio, M. C.; Ouerghi, A. Band alignment and minigaps in monolayer MoS2-graphene van der Waals heterostructures. *Nano Letters* **2016**, *16*, 4054–4061.

(22) Wilson, N. R.; Nguyen, P. V.; Seyler, K.; Rivera, P.; Marsden, A. J.; Laker, Z. P.; Constantinescu, G. C.; Kandyba, V.; Barinov, A.; Hine, N. D.; Xu, X.; Cobden, D. H. Determination of band offsets, hybridization, and exciton binding in 2D semiconductor heterostructures. *Science Advances* **2017**, *3*, e1601832.

(23) Hoesch, M. et al. A facility for the analysis of the electronic structures of solids and their surfaces by synchrotron radiation photoelectron spectroscopy. *Rev. Sci. Instrum.* **2017**, *88*, 013106.

(24) Wang, L.; Gutiérrez-Lezama, I.; Barreteau, C.; Ubrig, N.; Giannini, E.; Morpurgo, A. F. Tuning magnetotransport in a compensated semimetal at the atomic scale. *Nature Communications* **2015**, *6*, 8892.

(25) Mayorov, A. S.; Gorbachev, R. V.; Morozov, S. V.; Britnell, L.; Jalil, R.; Ponomarenko, L. A.; Blake, P.; Novoselov, K. S.; Watanabe, K.; Taniguchi, T.; Geim, A. K. Micrometer-scale ballistic transport in encapsulated graphene at room temperature. *Nano Letters* **2011**, *11*, 2396–2399.

(26) Zomer, P. J.; Guimarães, M. H. D.; Brant, J. C.; Tombros, N.; Van Wees, B. J. Fast pick up technique for high quality heterostructures of bilayer graphene and hexagonal boron nitride. *Applied Physics Letters* **2014**, *105*, 13101.

(27) Pletikosić, I.; Ali, M. N.; Fedorov, A.; Cava, R.; Valla, T. Electronic Structure Basis for the Extraordinary Magnetoresistance in WTe_2. *Phys. Rev. Lett.* **2014**, *113*, 216601.

(28) Kretinin, A. V. et al. Electronic properties of graphene encapsulated with different two-dimensional atomic crystals. *Nano Letters* **2014**, *14*, 3270–3276.

(29) Heyd, J.; Scuseria, G. E.; Ernzerhof, M. Hybrid functionals based on a screened Coulomb potential. *The Journal of Chemical Physics* **2003**, *118*, 8207–8215.

(30) Kresse, G.; Furthmüller, J. Efficient iterative schemes for ab initio total-energy calculations using a plane-wave basis set. *Phys. Rev. B* **1996**, *54*, 11169–11186.

(31) Choe, D.-H.; Sung, H.-J.; Chang, K. J. Understanding topological phase transition in monolayer transition metal dichalcogenides. *Physical Review B* **2016**, *93*, 125109.

(32) Liu, W. L. et al. Effect of aging-induced disorder on the quantum transport properties of few-layer WTe2. *2D Materials* **2017**, *4*, 011011.

(33) Woods, J. M.; Shen, J.; Kumaravadivel, P.; Pang, Y.; Xie, Y.; Pan, G. A.; Li, M.; Altman, E. I.; Lu, L.; Cha, J. J. Suppression of Magnetoresistance in Thin WTe 2 Flakes by Surface Oxidation. *ACS Applied Materials & Interfaces* **2017**, *9*, 23175–23180.

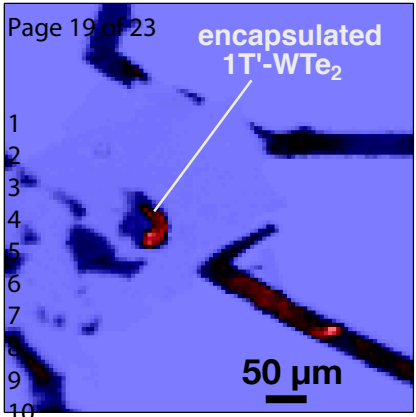

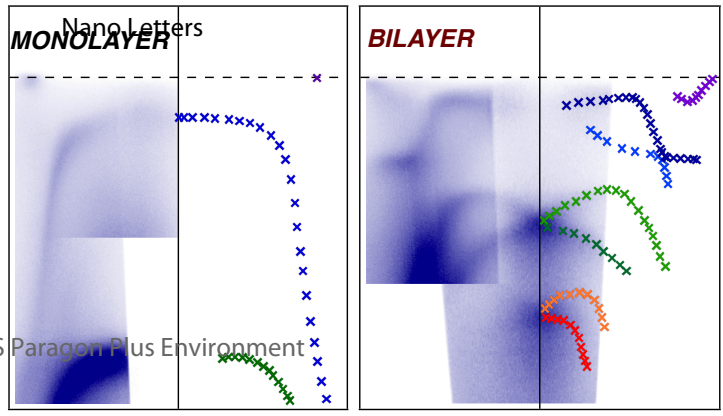

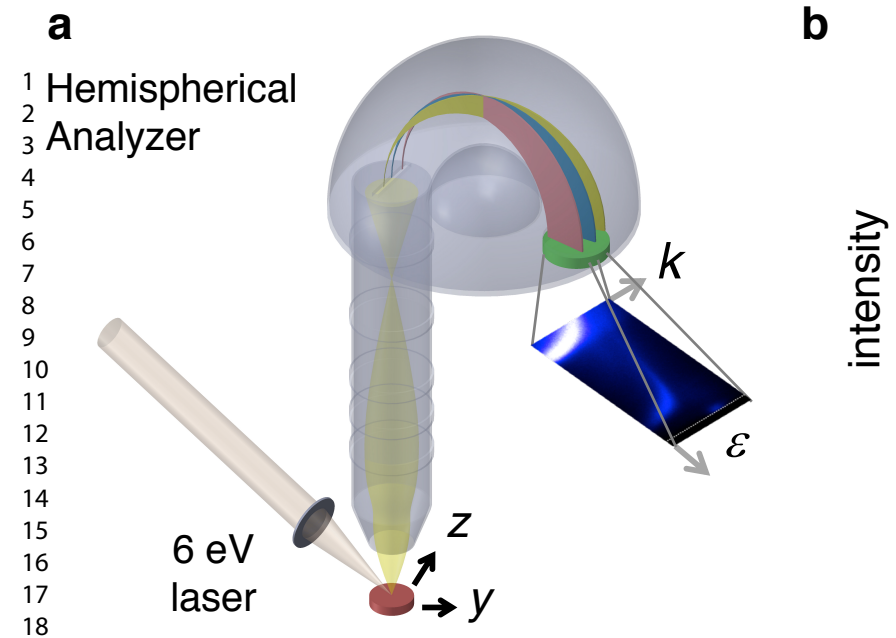
a
Hemispherical
Analyzer
k
ε
6 eV
laser
z
y

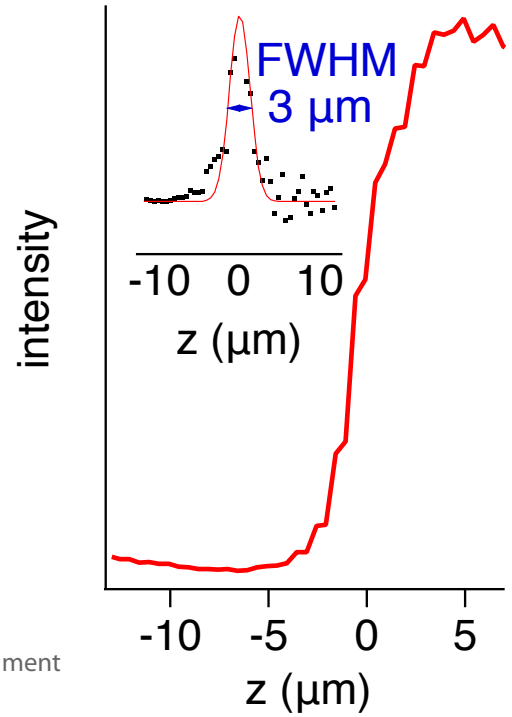
b
FWHM
3 µm
-10 0 10
z (µm)
intensity
-10 -5 0 5
z (µm)

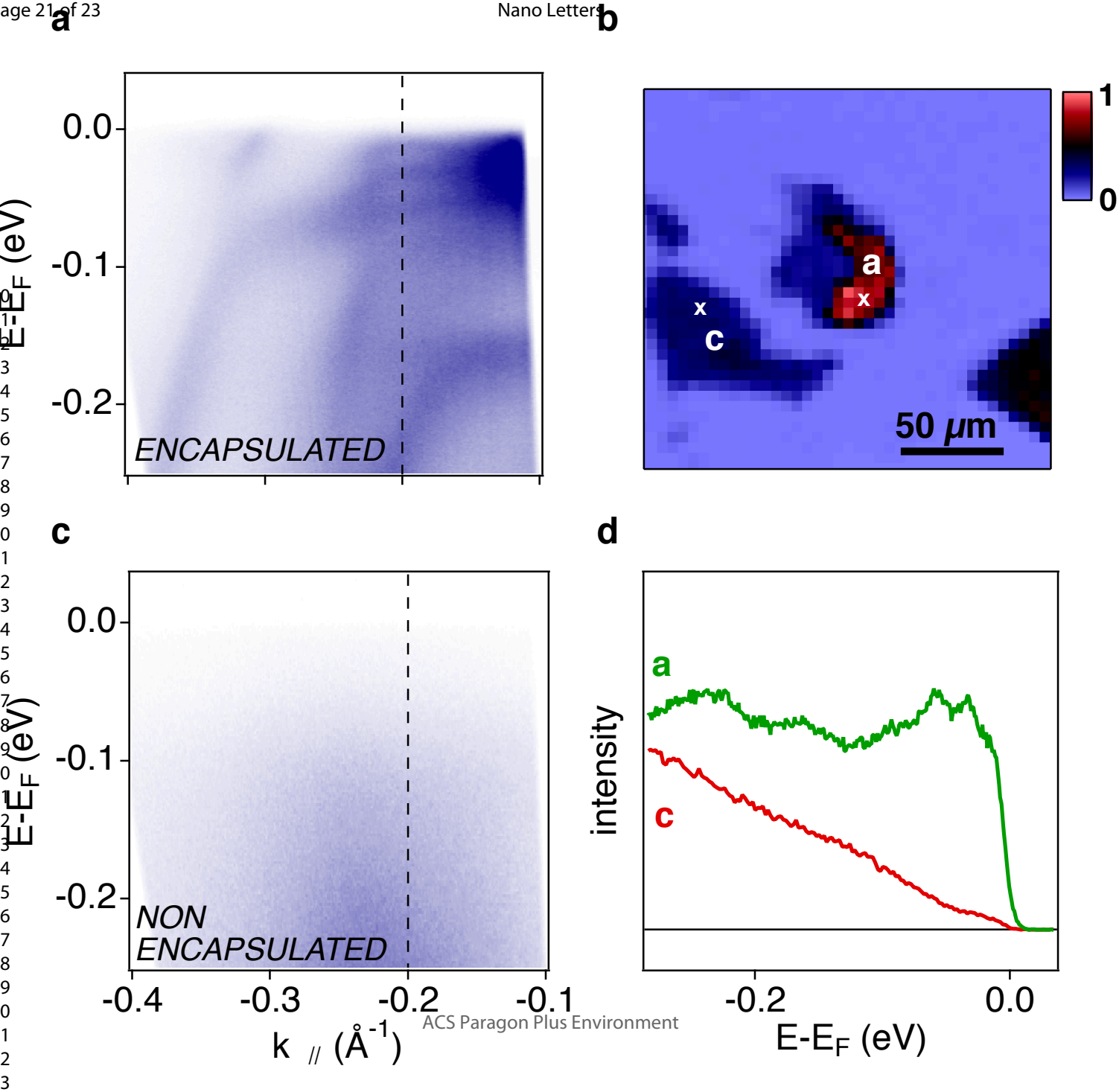
a
b
c
d
0.0
-0.1
-0.2
E-E$_F$ (eV)
ENCAPSULATED
1
0
a
x
x
c
50 μm
NON
ENCAPSULATED
-0.4
-0.3
-0.2
-0.1
k // (Å^{-1})
intensity
a
c
-0.2
0.0
E-E$_F$ (eV)

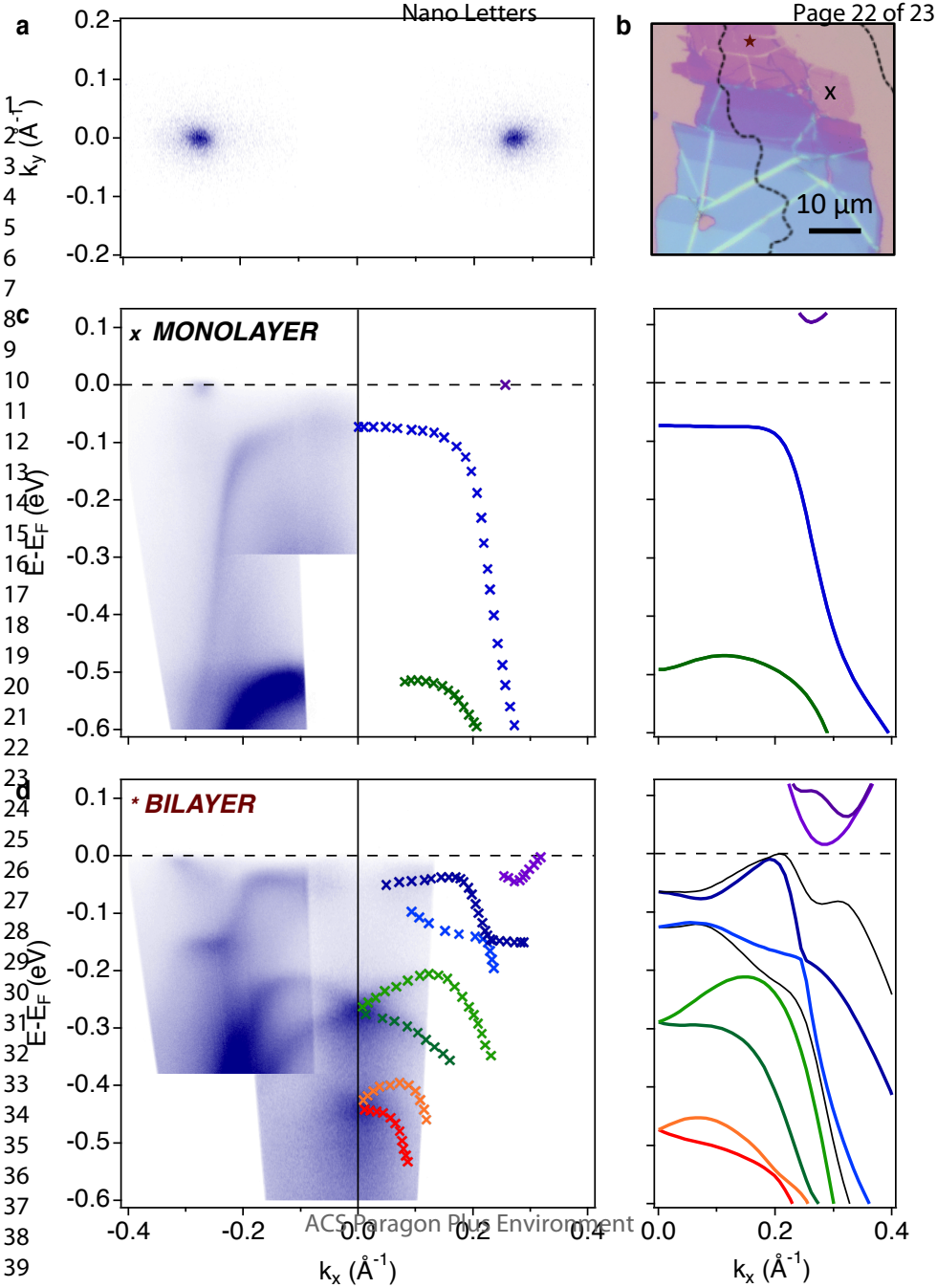

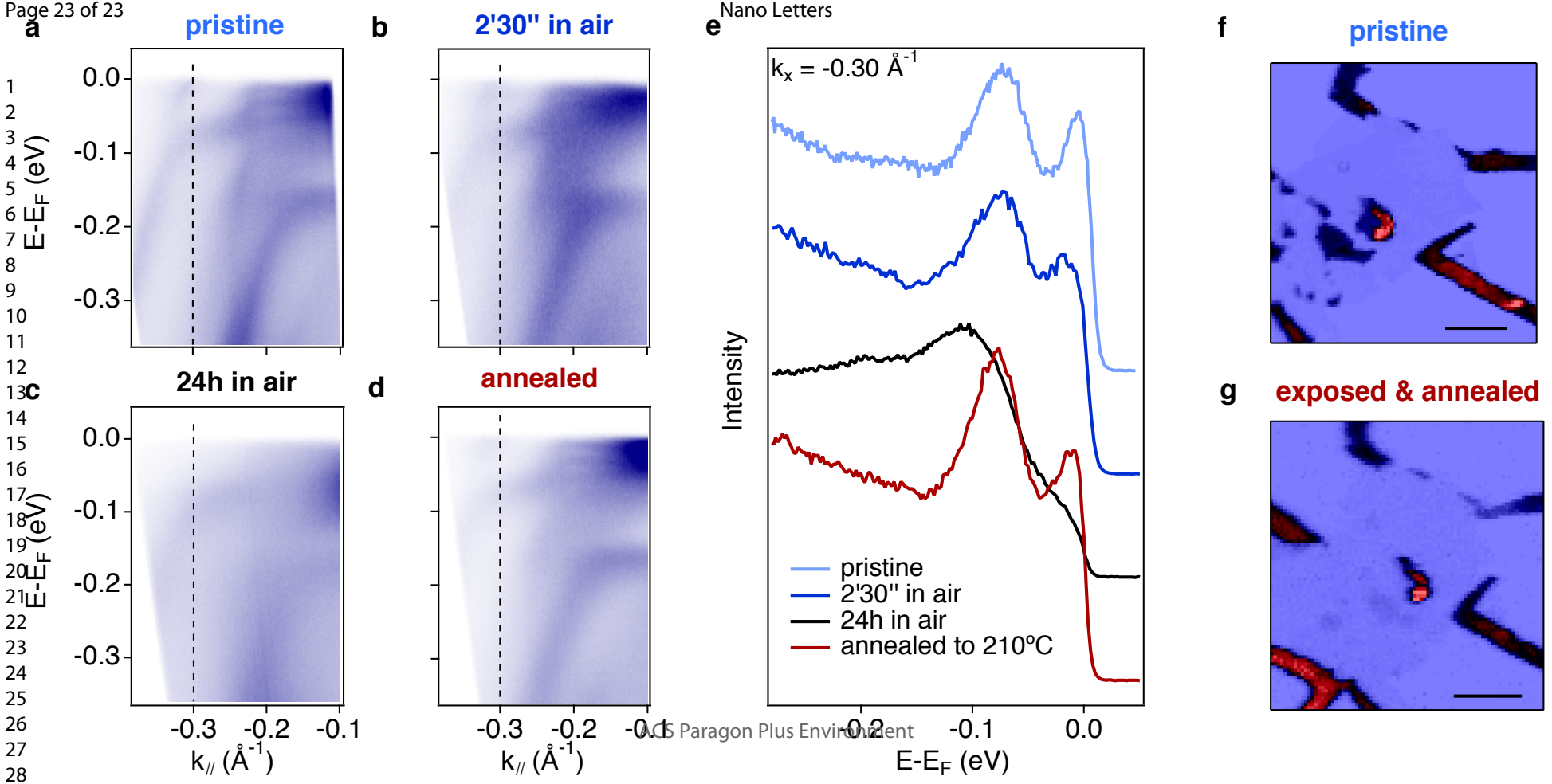
a
pristine
b
2'30'' in air
c
24h in air
d
annealed
E-E$_F$ (eV)
0.0
-0.1
-0.2
-0.3
-0.3
-0.2
-0.1
k$_{//}$ (Å^{-1})
e
k$_x$ = -0.30 Å^{-1}
Intensity
pristine
2'30'' in air
24h in air
annealed to 210°C
-0.2
-0.1
0.0
E-E$_F$ (eV)
f
pristine
g
exposed & annealed